

Ultrasonic defect characterization using Bayesian inversion and scattering matrix denoising neural networks

Changrong Guo, Junjie Ren, Jianfeng Xu, Long Bai *

State Key Laboratory of Digital Manufacturing Equipment and Technology, School of Mechanical Science and Engineering, Huazhong University of Science and Technology, Wuhan 430074, China

ARTICLE INFO

Keywords:

Crack-like defects
Distortion model
Bayesian inversion
Denoising neural network
Defect characterization
Scattering matrix

ABSTRACT

The use of scattering matrix and deep neural networks for ultrasonic characterization of inclined crack-like defects in noisy environments was explored. A distortion model was utilized to simulate coherent noises that could contaminate the experimental measurements in practice. Given a test scattering matrix, we first developed an approach for estimating the parameters of the distortion model based on the structural similarity index. Subsequently, a Bayesian inversion approach was adopted to determine the proportion of positive-angled cracks that should be included in the scattering matrix database. Based on this result, a deep neural network model was constructed and used in the denoising procedure, which can effectively reduce the characterization error induced by measurement noise. The simulation showed that the proposed approach can be reliably used for characterization of crack-like defects with large orientation angles relative to the array direction (e.g., 75°) and small sizes (e.g., 0.8λ). In experiments, six crack-like defects with orientation angles of 60° and 75° were characterized with errors within 0.1λ (i.e., 0.25 mm) and 5° in size and angle, respectively. In addition, the characterization uncertainty measured by the root-mean-squared error was reduced by 44.7% in size compared with the conventional Bayesian approach.

1. Introduction

Structural components can suffer serious consequences due to the presence of undetected defects [1], such as cracks. In the literature, a variety of methods have been developed for surface or near-surface crack detection, such as machine vision inspection [2] and deep-learning-based fluorescent magnetic particle inspection [3]. However, these methods lack the ability to detect internal cracks. For crack width assessment, distributed fiber optic sensors [4–6] can be used, which were shown to facilitate visualization of strains and cracks in building materials [7]. Eddy current pulsed thermography was applied to depth quantification of contact fatigue cracks by taking advantage of electromagnetic thermal execution [8]. In addition, non-destructive testing (NDT) techniques based on mechanical waves, such as acoustic emissions [9], make it possible to accurately identify and predict the growth of fatigue cracks.

Ultrasonic inspection is a popular NDT technique and is often used for structural safety monitoring [10]. Accurate characterization (i.e., determining the size and orientation angle) of crack-like defects is regarded as one of the main objectives of ultrasonic NDT [11], and many recent works have studied this problem in the NDT community [12–14]. A classic method for determining the size of defects in the

industry is the so-called 6-dB drop approach [15], which involves measuring the distance over which the A-scan amplitude drops by one-half from the peak value. In addition, ultrasonic imaging [16] is widely adopted for defect detection and characterization, empowered by advanced imaging algorithms such as the total focusing method (TFM) [17] and plane wave imaging (PWI) [18]. These imaging algorithms adopt an ultrasonic array data acquisition scheme known as full matrix capture (FMC) [17]. In an ideal UT scenario, it is possible to deduce the defect parameters directly from high-resolution ultrasonic images [19]. However, as the defect size approaches the ultrasonic wavelength, these methods were shown to encounter difficulty in distinguishing crack-like defects from other types of defects with similar sizes [20].

Two existing alternative approaches are capable of characterizing sub-wavelength defects: super-resolution imaging [21] and scattering-matrix-based inversion [22]. While the characterization performance of super-resolution imaging algorithms deteriorates dramatically as a crack becomes rough and inclined [21], the scattering-matrix-based approach has the potential to address this issue since it encodes all the scatterer information that can be extracted from the array data [23]. It was previously shown that the scattering matrix can be used for

* Corresponding author.

E-mail addresses: guochangrong@hust.edu.cn (C. Guo), renjunjie0121@163.com (J. Ren), jfxu@hust.edu.cn (J. Xu), bailong@hust.edu.cn (L. Bai).

accurate characterization of crack-like defects by adopting a nearest neighbor (NN) approach, given that defects are favorably oriented [24]. Velichko et al. [25] generalized this approach by introducing the defect manifold and proposed a Bayesian approach for quantifying the characterization uncertainty. By introducing a coherent noise model, it was concluded by the authors that the characterization uncertainty becomes high for inclined defects because their scattering matrices are more easily affected by noise [25]. In order to improve the characterization results of such inclined defects, this study noted that the key is to recover a noise-free version of the scattering matrix from the one distorted by noise and use the former for characterization. In previous studies, Bai et al. [24] adopted principal component analysis (PCA) to reduce the effect of measurement noise and recover the original shape of the scattering matrix from noisy data. Velichko et al. [25] proposed a parametric manifold mapping approach (PMMA) for defect characterization using scattering matrices, and noise reduction was achieved by projecting the measured data onto a noise-free defect manifold. However, the characterization performance of both approaches deteriorated when the crack-like defects are unfavorably oriented.

Deep learning approaches, such as deep convolutional neural networks (CNNs), have been widely used for image denoising. Many CNN-based denoisers, such as DnCNN [26], FFDNet [27] and CBDNet [28], were proposed for the removal of additive white Gaussian noise (AWGN) and more sophisticated noises in a real camera system (e.g., dark current noise, short noise, and thermal noise) [28]. The application of deep CNNs in the field of NDT for defect detection and localization can also be found in the literature. For example, Gao et al. [29] showed that informative features can be extracted from Lamb wave signals by fusing the CNN and stack autoencoder (SAE). Miorelli et al. [30] proposed an automatic defect localization and sizing procedure for guided wave imaging using CNNs. The characterization performances of Bayesian inversion and deep neural networks were compared using the scattering matrix in Ref. [20], but it only studied the effect of coherent noise on the characterization accuracy and did not provide an approach to minimize the effect of noise.

Previous studies have shown excellent promise in scattering matrices and deep learning. However, the characterization of inclined cracks with large angles remains a significant challenge consisting of two parts: (1) it is unclear how to accurately estimate the noise level of an experimentally-measured scattering matrix, and (2) it is difficult to remove structural noise from noisy scattering matrices using the aforementioned conventional denoising methods. Faced with these difficulties, this study proposes a hybrid approach combining a Bayesian approach with a deep neural network for denoising of scattering matrices. The objectives of this paper are as follows: (1) to design a dedicated neural network structure suitable for scattering matrix denoising, (2) to reduce the uncertainty in the characterization of inclined cracks, and (3) to develop a practical characterization procedure that is applicable to experimental data measured in noisy environments.

Unlike the aforementioned PCA- and PMMA-based noise reduction approaches, which are formulated using a noise-free scattering matrix database of idealized reference defects, the proposed hybrid approach that combines the Bayesian inversion with deep neural networks can learn from both defect data (i.e., noise-free scattering matrix) and noise data (i.e., multiple realizations of coherent noise). Thus, it can provide improved noise reduction performance, particularly for unfavorably oriented cracks. First, we introduce the distortion model; then, PMMA and the mean structural similarity index (MSSIM) are combined to achieve an accurate estimation of the noise parameters. Finally, Bayesian inversion is used for the initial classification of crack angles to reduce the complexity of fitting the proposed scattering matrix denoising neural network (SMDNet) to the data. This work has practical implications for reducing the characterization uncertainty of unfavorably oriented defects and can help enhance the capability of characterizing inclined cracks with ultrasonic arrays.

The remainder of this paper is organized in Sections 2–5. In Section 2, we introduce the scattering matrix, Bayesian approach, and SMDNet based on U-net [31]. The characterization performances of different approaches on the simulation data are compared in Section 3. The proposed denoising procedure is applied to the experimental data, and the results are presented in Section 4. Finally, the conclusions are located in Section 5.

2. Methodology

2.1. The Bayesian approach based on the scattering matrix

The interaction between ultrasonic waves and defects can be described by an ultrasonic scattering matrix, which consists of far-field scattering coefficients for different incident-scattering angle pairs [22]. Fig. 1 shows a schematic diagram with the geometry used in the scattering matrix definition. The far-field scattering matrix (only longitudinal waves are considered here) is defined in a 2-dimensional scenario as [22]:

$$S(\theta_1, \theta_2, \omega) = \frac{a_{sc}(\omega)}{a_{in}(\omega)} \sqrt{\frac{d_{sc}}{\lambda}} \exp\left(-\frac{i\omega d_{sc}}{c}\right) \quad (1)$$

where θ_1 and θ_2 are the incident and scattering angles (see Fig. 1), respectively, a_{in} is the amplitude of the plane incident wave, and a_{sc} is the amplitude of the scattered wave measured at a distance d_{sc} from the defect. In addition, c is the longitudinal wave speed, ω is the angular frequency, and $\lambda = 2\pi c/\omega$ is the wavelength of longitudinal waves.

As stated in Ref. [32], an experimental scattering matrix is often contaminated by the distortion \mathbf{n}_p which is defined as the difference between the experimental measurement \mathbf{s}_n and the ideal scattering matrix \mathbf{s}_p , i.e.:

$$\mathbf{s}_n = \mathbf{s}_p + \mathbf{n}_p \quad (2)$$

In Eq. (2), the subscript p denotes parameters of a defect, such as size and orientation angle. The distortion consists of noise from different sources, including defect roughness, material noise, and the interference from geometric features. The general coherent noise model [25] can be used to simulate distortions as two-dimensional Gaussian rough surfaces [33]. The RMS roughness σ , and the correlation lengths λ_1 , λ_2 , can be used to define the distortion model. A random realization of distortion can be obtained using this model as:

$$\mathbf{n}_{gen}(\theta_1, \theta_2) = (c(\theta_1, \theta_2) \otimes \mathbf{n}_g(\theta_1, \theta_2) - \mu') \frac{\sigma}{\sigma'} \quad (3)$$

where \otimes is the convolution operator, and μ' and σ' denote the mean and standard deviation of the convolution term $c \otimes \mathbf{n}_g$, respectively. In addition, \mathbf{n}_g is the uncorrelated unit variance and zero mean Gaussian white noise, and the correlation function c is defined as:

$$c(\theta_1, \theta_2) = \exp\left(-\frac{\varphi_1^2}{\lambda_1^2} - \frac{\varphi_2^2}{\lambda_2^2}\right) \quad (4)$$

In Eq. (4), a rotation operator parameterized by ϕ , which is set as -45° in this study considering the diagonal patterns of scattering matrices, is applied to the pair of variables (θ_1, θ_2) as follows:

$$\begin{pmatrix} \varphi_1 \\ \varphi_2 \end{pmatrix} = \mathbf{R} \begin{pmatrix} \theta_1 \\ \theta_2 \end{pmatrix}, \quad \mathbf{R} = \begin{pmatrix} \cos \phi & \sin \phi \\ -\sin \phi & \cos \phi \end{pmatrix} \quad (5)$$

Fig. 2(a) shows the experimentally measured scattering matrix of a 1.6λ , 75° crack. By comparing this result with the noise-free scattering matrix in Fig. 2(b), it can be seen that the experimental noise (Fig. 2(c)) is coherent and cannot be removed by averaging or filtering operations. This necessitates the use of the distortion model described above for characterization and uncertainty analysis. Fig. 2(d) shows a random realization of the simulated noise obtained using the distortion model. The parameters of the distortion model include RMS roughness $\sigma = 0.05$, and correlation lengths $\lambda_1 = 30^\circ$ and $\lambda_2 = 40^\circ$.

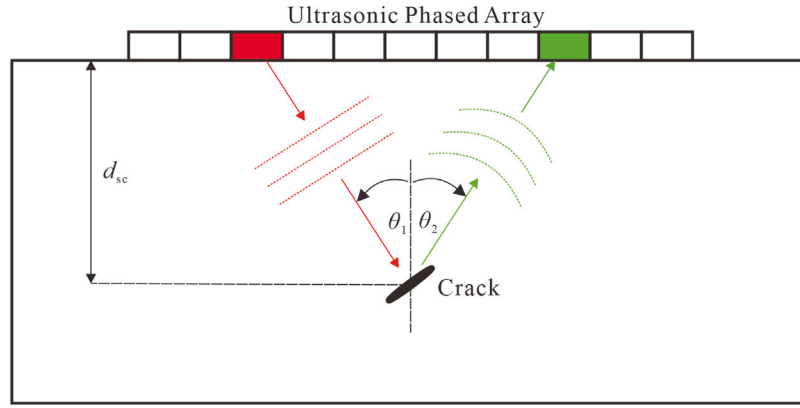


Fig. 1. Array measurement configuration used for extracting the scattering matrix of a crack-like defect; θ_1 and θ_2 are defined with respect to the vertical direction and take positive values if they are measured clockwise.

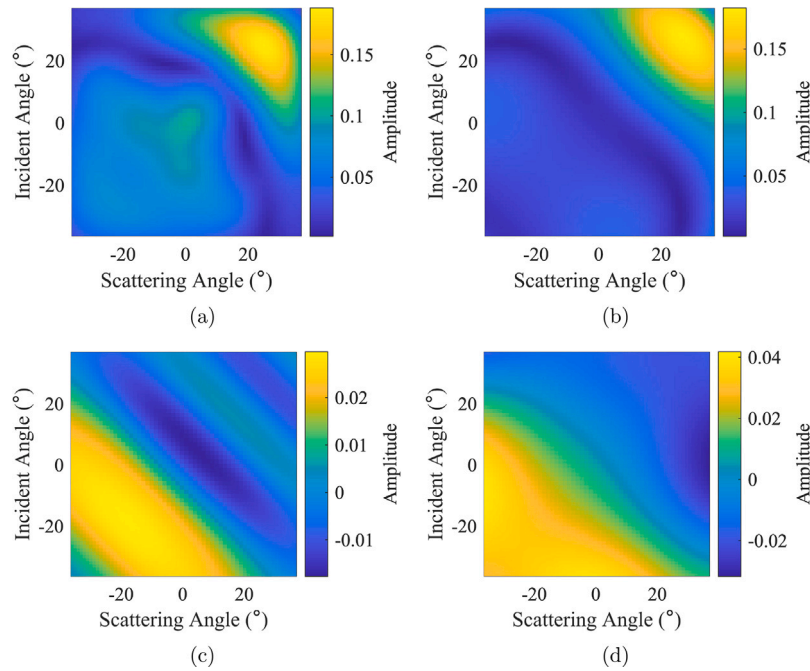


Fig. 2. (a) Experimentally measured scattering matrix of a 1.6λ , 75° crack, (b) the noise-free scattering matrix, (c) experimental noise, and (d) a random realization of coherent noise obtained using the distortion model.

With the introduction of the distortion model, the defect characterization result is given by the Bayesian approach as the conditional probability $P(p|s_n)$. More specifically, this is the probability of the defect parameter p given the experimental data s_n [25]. Based on Bayes' theorem [34], it can be calculated from:

$$P(p|s_n) = \frac{P(s_n|p)P(p)}{P(s_n)} \quad (6)$$

For simplicity, it is assumed that the prior probability of defect parameter $P(p)$ and scattering matrix $P(s_n)$ are constant. These quantities could potentially take different values as well, if additional information about the experimental setup is available [25]. By further assuming that the probability of noise $P(n_p)$ is independent of the defect parameter p and scattering matrix s_p , the characterization result can be simplified as:

$$P(p|s_n) = CP(n_p) \quad (7)$$

where C is a normalization constant. The final characterization result of the Bayesian approach can be presented as a probability map

which shows conditional probability values for different defect parameters [25].

Although it has a high characterization accuracy for favorably oriented defects, the Bayesian approach also suffers from high characterization uncertainty and large errors when characterizing cracks that are steeply inclined. In addition, the performance of the Bayesian approach is also dependent on the parameters of the distortion model, hereafter referred to as the noise parameters, because different noise parameters also mean different noise distributions $P(n_p)$ (Eq. (7)). Fig. 3(a) shows the characterization result of the Bayesian approach for a 1.6λ , 75° crack (see Fig. 2(a) for the noisy scattering matrix), obtained when the actual noise parameters were used for characterization. In Fig. 3(b), a different set of noise parameters (RMS roughness $\sigma = 0.05$ and correlation lengths $\lambda_1 = 15^\circ$, $\lambda_2 = 15^\circ$) are used when calculating the probability map result; the true parameter point shown as the red dot suggests that the sizing error is large. On the other hand, while exhibiting a significant degree of uncertainty in defect size, it can be concluded from Fig. 3 that the Bayesian approach performs well when estimating the orientation angle of a defect. For this reason, it is used

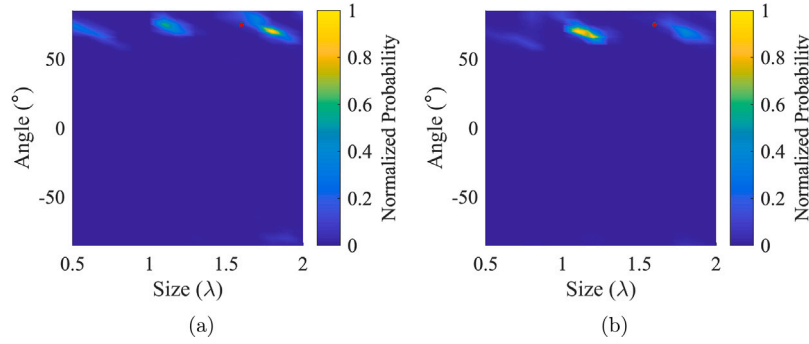


Fig. 3. Characterization results of the Bayesian approach for a 1.6λ , 75° crack containing noise: (a) correct noise parameters, and (b) incorrect noise parameters are used for characterization. The color bars show the normalized probability and the red dots denote the true defect parameters. (For interpretation of the references to color in this figure legend, the reader is referred to the web version of this article.)

in Section 4 to determine the proportion of positive-angled cracks in the scattering matrix database for training the deep denoising neural network.

2.2. Deep denoising neural network

Here, we take a different perspective on the defect characterization problem described in Section 2.1. As mentioned in Section 1, the key to accurate defect characterization in noisy environments is denoising, in other words, reconstructing a noise-free scattering matrix \hat{s}_p from the noisy measurement s_n . The nearest neighbor method can then be adopted to find the best match in the set of reference scattering matrices (i.e., the defect database). A deep neural network model for processing noisy scattering matrices is introduced. In the following passages, this model is termed ‘a scattering matrix denoising network’ (SMDNet).

The U-net architecture [31] is used as the backbone for the proposed SMDNet. Full convolutional networks (FCN) are known to achieve pixel-level predictions by removing the fully-connected layers of conventional CNNs [35]. The U-net is a variant of FCN which was first proposed in Ref. [31] for biomedical image segmentation. It consists of a symmetrical encoder–decoder structure. The encoder compresses the image dimensions by convolution and down-sampling, while the decoder recovers the original image resolution through up-sampling and skip-connections [31]. Both global and local features can be integrated with these operations; as a result, the U-net has stronger pixel-level nonlinear mapping capabilities than FCN. The U-net structure was used as the backbone of recent image denoising networks based on convolution [36–38] and vision transformer [39,40]. Various feature extraction modules were added on this basis. In addition, Zhang et al. showed that using noise images and noise estimation maps as inputs of the U-net improved the generalizability of the model [26]. A denoiser called CBDnet was developed by the authors based on an FCN-Unet architecture for image denoising [28]. In this study, it is noted that the U-net is well suited for learning the mapping between the noisy and noise-free scattering matrices. Moreover, the FCN of the CBDnet is replaced by another U-net for better noise estimation performance, and hence, a Unet-Unet architecture has been obtained for the proposed SMDNet.

As shown in Fig. 4, the SMDNet consists of a noise estimation network U-net_N and a denoising network U-net_D; the two U-nets have the same number of hidden layers but different input layers (one feature map for U-net_N as opposed to two for U-net_D). The supplemental materials include additional details. The U-net_N takes a noisy scattering matrix s_n as an input and generates an estimated noise map $\hat{n}(s_n) = f_N(s_n; \mathbf{w}_N)$, where \mathbf{w}_N represents the network parameters. Following this, U-net_D takes both s_n and $\hat{n}(s_n)$ as the inputs and the final denoised scattering matrix is obtained as $\hat{s}_p = f_D(s_n; \hat{n}(s_n); \mathbf{w}_D)$, where \mathbf{w}_D are parameters of U-net_D. Convolution is the key operation of the encoder

Table 1

Specifications of the array transducer used in simulation and experiments.

Parameter	Value
Number of elements	64
Element width (mm)	0.35
Element pitch (mm)	0.5
Element length (mm)	15
Central frequency (MHz)	2.5

part of the SMDNet, and an output convolutional feature \tilde{X} can be computed from feature X of the previous layer as follows:

$$\tilde{X} = \sigma(W_{3 \times 3} \otimes X) \quad (8)$$

In Eq. (8), σ is the ReLU activation function, \otimes is the convolution operator, and the subscript of $W_{3 \times 3}$ is used to indicate the filter size. Also, $X = [x_1, x_2, \dots, x_{N_{in}}] \in \mathbb{R}^{N_{in} \times H_{in} \times W_{in}}$ denotes the input data of a convolutional layer, with $H_{in} \times W_{in}$ acting as the dimensions of the input feature and N_{in} representing the number of feature maps. Because the phase measurement is highly sensitive to localization errors [25], only the amplitude of the scattering matrix is considered in this paper. Since a 2.5 MHz, 64-element array is used in the simulation and experiments of this study (see Table 1), the input and output layers of the proposed SMDNet both have dimensions of $1 \times 64 \times 64$. The number of feature map channels of each layer is shown in Fig. 4. In order to remove redundant information and enlarge the receptive field, 2×2 average pooling layers (AvgPool2d) were used to compress the length and width of the feature maps by one half.

The decoder part of the proposed SMDNet is characterized by skip-connection and transposed convolution processes. Skip-connection is used to add feature maps of the encoder to those of the decoder with the same dimensions, and up-sampling is achieved by the transposed convolution. This process can be expressed as follows:

$$\tilde{Z} = \sigma(W_{2 \times 2} \otimes' Z + I) \quad (9)$$

where \otimes' denotes the transposed convolution, I is the feature map of the encoder that is connected to the decoder, and Z and \tilde{Z} are the input and output features, respectively.

The objective function of the SMDNet is composed of the noise estimation loss \mathcal{L}_{est} and scattering matrix reconstruction loss \mathcal{L}_{rec} , which quantify the learning performance of its two sub-networks. The noise estimation loss \mathcal{L}_{est} is defined as:

$$\mathcal{L}_{est} = \sum_i \left| k_1 - \mathbb{I}_{\hat{n}(s_{n,i}) - n(s_{n,i})} \right| \cdot (\hat{n}(s_{n,i}) - n(s_{n,i}))^2 \quad (10)$$

where $\hat{n}(s_{n,i})$ and $n(s_{n,i})$ are the estimated and ground truth values of noise at pixel i , respectively, and \mathbb{I} is defined as:

$$\mathbb{I}_\alpha = \begin{cases} 0, & \text{for } \alpha < 0 \\ 1, & \text{otherwise} \end{cases} \quad (11)$$

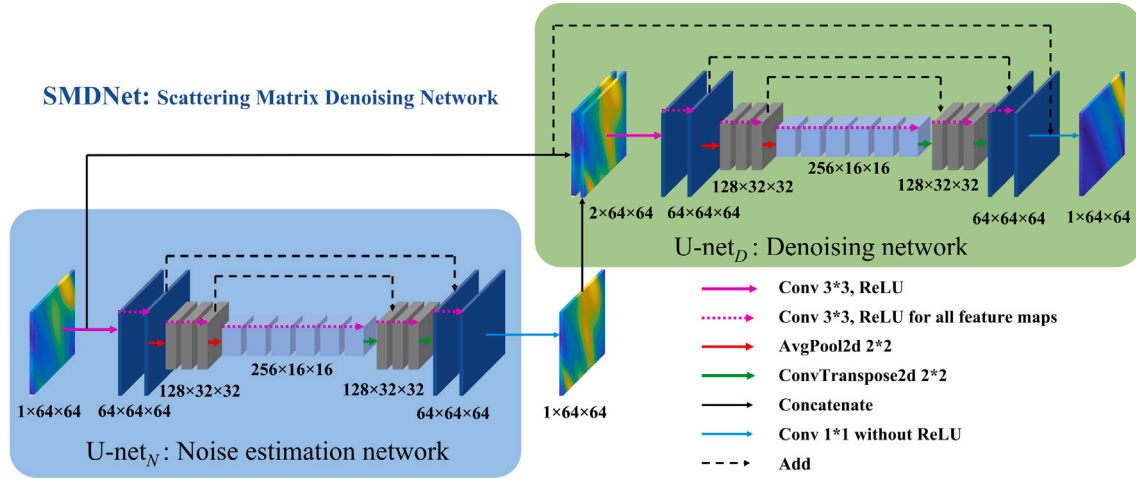


Fig. 4. Architecture of the scattering matrix denoising networks (SMDNet).

Table 2

Hyperparameters of the SMDNet.

Hyperparameter	Value
Batch size	32
Learning rate	0.001
Epoch	100
Early-stopping patience	10
k_1, k_2 (see Eqs. (10) and (12))	0.3, 0.3
β (see Eq. (13))	0.5

It can be seen from Eqs. (10)–(11) that the SMDNet adopts an asymmetric loss [28]. This is necessary because the amplitudes of the noise-free scattering matrices are small for the studied problem, and overestimating the noise or, underestimating the scattering amplitude of a defect, would normally cause larger errors than underestimating it. In Eq. (10), k_1 can be set as a value in the range (0, 0.5), which ensures that it will impose larger penalties when the noise value is overestimated, i.e., $\hat{n}(s_{n,i}) > n(s_{n,i})$. Similarly, we define the scattering matrix reconstruction error as:

$$\mathcal{L}_{rec} = \sum_i \left| k_2 - \mathbb{I}_{s_{p,i} - \hat{s}_{p,i}} \right| \cdot (\hat{s}_{p,i} - s_{p,i})^2 \quad (12)$$

where $k_2 \in (0, 0.5)$, and $\hat{s}_{p,i}$ and $s_{p,i}$ are the estimated and true values of the scattering matrix at pixel i . The overall loss function of the proposed SMDNet can be written as:

$$\mathcal{L} = \mathcal{L}_{rec} + \beta \cdot \mathcal{L}_{est} \quad (13)$$

where β is a trade-off parameter which determines the relative importance of the noise estimation loss. Following a grid search approach, the optimal values of β , k_1 , and k_2 were obtained as 0.5, 0.3, and 0.3, respectively.

During the training process, an Adam optimizer with a learning rate set to 0.001 was employed to optimize the network weights and biases on an Nvidia GeForce GTX 1060 6G GPU. The size of the mini-batch was 32, and an early stop was applied to address the over-fitting issue once the validation loss failed to improve after ten iterations. It took on average of 1.94 h to train the SMDNet with the Pytorch package. The hyperparameters are listed in Table 2, and the supplemental materials include the optimization details.

For quantitative evaluation of the characterization performance, several standard error metrics were used on the predictions, namely, the root mean square error (RMSE), R^2 score, mean absolute error (MAE), and explained variance score (EVS), which are defined as follows:

$$RMSE_i = \sqrt{\frac{1}{K} \sum_{k=1}^K (\hat{p}_{ki} - p_{ki})^2}, \quad i = 1, 2 \quad (14)$$

$$R^2_i = \frac{\sum_{k=1}^K (\hat{p}_{ki} - \bar{p}_i)^2}{\sum_{k=1}^K (p_{ki} - \bar{p}_i)^2}, \quad i = 1, 2 \quad (15)$$

$$MAE_i = \frac{1}{K} \sum_{k=1}^K |\hat{p}_{ki} - p_{ki}|, \quad i = 1, 2 \quad (16)$$

$$EVS_i = 1 - \frac{\text{Var}\{\hat{p}_{ki} - p_{ki}\}}{\text{Var}\{p_{ki}\}}, \quad i = 1, 2 \quad (17)$$

where \hat{p}_{ki} ($i = 1, 2$) denotes the predicted crack size and angle, respectively, p_{ki} ($i = 1, 2$) are the true defect parameters, and \bar{p}_i ($i = 1, 2$) are the average values of p_{ki} ($i = 1, 2$). ‘Var’ means the variance, and K is the number of test samples.

3. Simulation results

3.1. Database preparation and implementation of the SMDNet

A 2.5 MHz, 64 element array with an element pitch of 0.5 mm was used in the simulation and experiments included in this study. The inspection material was assumed to be aluminum (Young’s modulus = 69 GPa, Poisson’s ratio = 0.334, and density = 2700 kg m⁻³). A noise-free scattering matrix database was prepared by simulating the scattering matrices of cracks using an analytically based computer model [41]. Ideal scattering matrices are simulated for incident and scattering angles between -90° and 90° , which represent the maximum amount of information extractable from a one-sided measurement. The forward simulations were performed at the center frequency of 2.5 MHz, and the considered size range was between 0.5λ (i.e., 1.25 mm) and 2λ (i.e., 5 mm). The orientation angle range considered was between -85° and 85° . A positive value means that it is measured clockwise from the array direction. The SMDNet is introduced in this study specifically for the characterization of unfavorably oriented cracks, which can be generally described as cracks having orientation angles greater than 45° for the measurement configuration adopted in this paper. Because both positive and negative orientation angles are possible in practice, database cracks were split into two groups according to their orientations, i.e., $(50^\circ, 85^\circ)$ and $(-85^\circ, -50^\circ)$, to explore the effects of the database composition (i.e., different proportions of positive- and negative-angled cracks) on the characterization performance of the SMDNet. The sampling intervals of the crack size and angle were selected as 0.1λ (i.e., 0.25 mm) and 5° , respectively.

The dataset used for training the SMDNet was prepared for a specific set of noise parameters. The validation and test sets were obtained using the same noise parameters but with different realizations of noise obtained with the distortion model. More specifically, a simulated noise

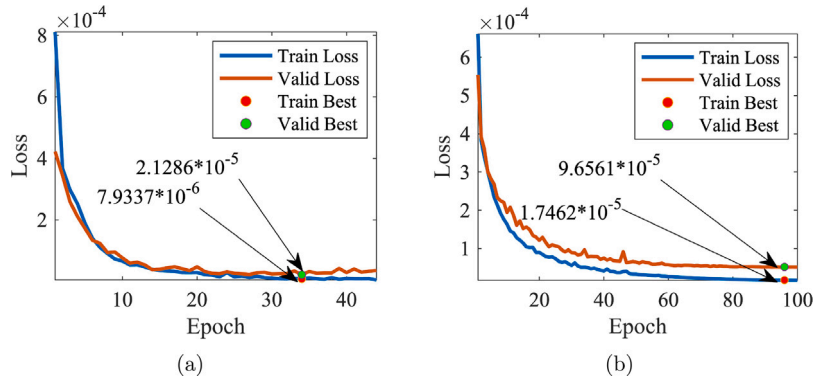


Fig. 5. The training and validation losses of the SMDNet obtained using different proportions of positive-angled cracks in the database: (a) positive angles only, and (b) 50% positive angles and 50% negative angles.

Table 3

Details of the data sets prepared for the SMDNet.

Dataset	Size (wavelengths)		Angle (degrees)		Number of samples
	Range	Interval	Range	Interval	
Training	From 0.5	0.1	From 50	5	$128 \times 50 = 6400$
Validation	to 2.0		to 85		$128 \times 20 = 2560$
Test					$128 \times 30 = 3840$

Table 4

The error metrics of size prediction for different methods.

Method	R2	MAE (λ)	RMSE (λ)	EVS
PCA [24]	0.0783	0.2844	0.4426	0.1051
PMMA [25]	0.1231	0.2811	0.4317	0.1601
NAFNet [38]	0.6216	0.1201	0.2836	0.6271
CBDNet [28]	0.9917	0.0046	0.0421	0.9917
SMDNet	0.9881	0.0053	0.0503	0.9881

Table 5

The error metrics of angle prediction for different methods.

Method	R2	MAE ($^\circ$)	RMSE ($^\circ$)	EVS
PCA [24]	0.5662	4.8138	7.5454	0.5667
PMMA [25]	0.5586	4.9453	7.6112	0.5641
NAFNet [38]	0.8342	2.3151	4.6645	0.8344
CBDNet [28]	0.9913	0.1745	1.0704	0.9913
SMDNet	0.9919	0.1732	1.0301	0.9919

n_{cor} can be added to an ideal noise-free scattering matrix s_{truth} to form a noisy sample s_{noisy} as follows:

$$s_{noisy} = s_{truth} + n_{cor} \quad (18)$$

The noise database $N_{cor} = [n_{cor,1}, n_{cor,2}, \dots, n_{cor,j}]$ contains $j = 50, 20, 30$ random noise realizations for training, validation, and test sets, respectively. The noise-free scattering matrix database $S_{truth} = [s_{truth,1}, s_{truth,2}, \dots, s_{truth,l}]$ consisted of $l = 16 \times 8 = 128$ (16 different sizes and 8 different angles) noise-free scattering matrices of positive-angled cracks. We also studied the performance of datasets with different compositions; l equals 256 in this case (i.e., the noise-free database contains both positive- and negative-angled cracks). Following this, the size m of the training, validation, and test sets can be calculated as $m = l \times j$, (i.e., each pair of simulated noise and noise-free scattering matrix yields a data sample — see Table 3).

Figs. 5(a)–(b) show the training and validation losses of the SMDNet obtained for different database compositions; the model reached convergence in both cases within 100 epochs.

3.2. Characterization performance of the SMDNet

As an illustrative example demonstrating the characterization performance of the SMDNet, the training, validation, and test sets were prepared by using coherent noise realizations obtained with the noise parameters $\sigma = 0.05$ and $\lambda_1 = \lambda_2 = 40^\circ$. The test scattering matrices were first denoised by the proposed SMDNet, and then the nearest neighbor method was applied to the denoised scattering matrices to obtain the final characterization result.

Figs. 6(a)–(b) show the RMSE results in size and orientation angle, respectively. They were obtained with training sets containing positive-angled cracks only. The negative-angled cracks that may be contained within the database have a negative impact on characterization performance; unstable results may occur (see Figs. 6(c)–(d)). Because scattering matrices of positive- and negative-angled cracks have different structures, it is difficult for the SMDNet to find an optimal solution that retains the most information-rich parts of both kinds of cracks. For example, the informative part of a positive-angled crack may be seen as noise for negative-angled cracks. For this reason, we used the Bayesian approach as a first step towards characterization in Section 4, which determines the appropriate database composition for a test scattering matrix.

As a comparison, Figs. 6(e)–(f) show the RMSE results obtained when principal component analysis (PCA) [42] was used for denoising (see Ref. [24] for details of this approach). It demonstrates that the SMDNet provides notably better predictions compared to PCA. After denoising, both methods adopted the nearest neighbor method for defect characterization. It is evident that the RMSE of the SMDNet is much lower than that of the PCA-based-denoising. It was reduced by 0.372λ and 6.679° on average for the size and angle parameter, respectively, except for cracks with extremely small sizes (0.5λ) and/or large orientation angles (85°). Hence, it is suggested that the SMDNet has the ability to reduce the characterization uncertainty of experimental data, which will be discussed further in Section 4.

The error metrics for the size and angle predictions of PCA [24], PMMA [25], NAFNet [38] (state of the art in image denoising in 2023), CBDNet [28], and SMDNet on simulated data are listed in Tables 4 and 5. They show that noise-estimation-network-based methods outperformed conventional denoising methods owing to their strong nonlinear fitting capabilities. Moreover, CBDNet and SMDNet achieved better predictions compared to NAFNet. It is noted that NAFNet suffers from an over-fitting issue since it did not include a noise estimation network; specifically, it was not built using the ‘learn-from-noise’ scheme. Furthermore, Tables 6 and 7 show that SMDNet achieved superior or similar prediction performance compared to CBDNet on different sets of noise parameters by replacing the FCN of CBDNet with a U-net structure, which provided better noise estimation performance.

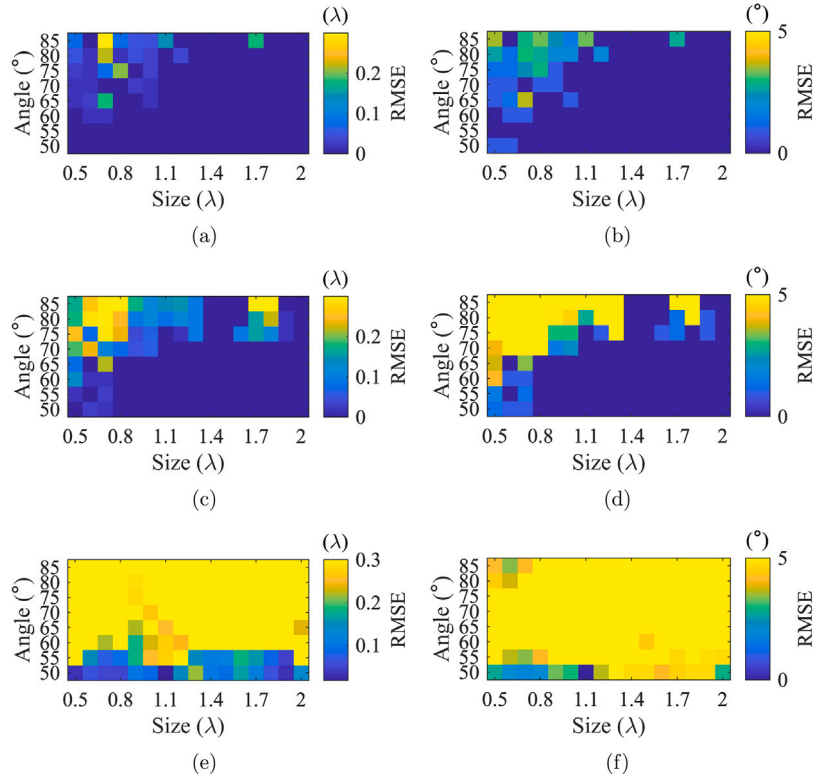


Fig. 6. RMSE of the characterization results of positive-angled test cracks with noise that were obtained with SMDNets trained using different proportions of positive-angled cracks — (a)–(b) positive angles only, and (c)–(d) 50% positive angles and 50% negative angles. In (e)–(f), only positive-angled cracks were included in the defect database, and PCA was adopted for denoising [24]. The left and right columns show results in size and angle, respectively.

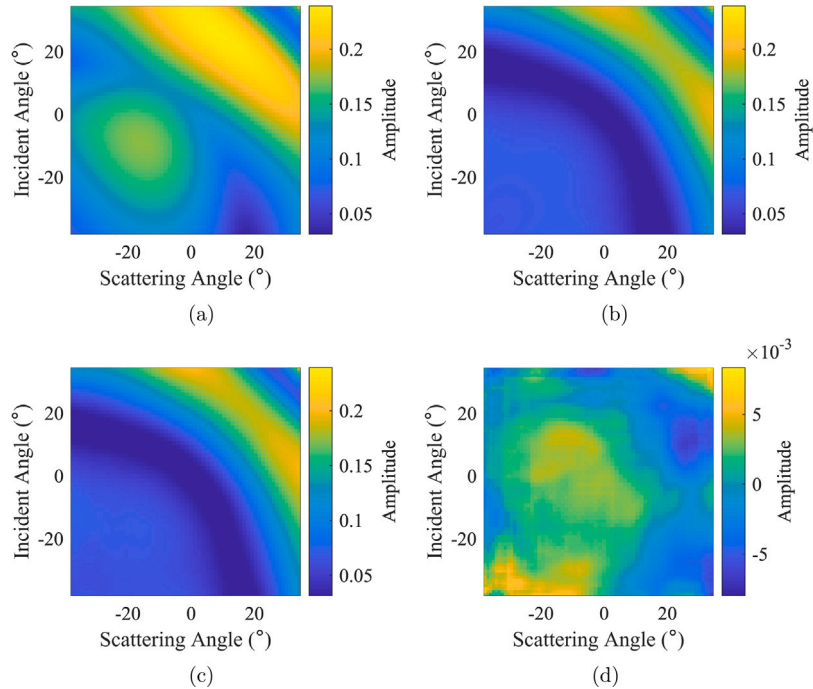


Fig. 7. (a) The noisy scattering matrix of a 1.2λ , 60° crack, (b) ideal scattering matrix, (c) denoised result, and (d) the reconstruction error.

Fig. 7(a) shows a simulated scattering matrix of a 1.2λ , 60° crack contaminated with noise. It shows that the added coherent noise distorted the structural information of the ideal scattering matrix (see **Fig. 7(b)**). The characterization result of the nearest neighbor approach

would be 1.3λ , 55° in this case. **Fig. 7(c)** shows the denoising result of the proposed SMDNet from which one can see that the coherent noise is suppressed and the shape and amplitude of the scattering matrix are well restored. The size and angle can be characterized accurately

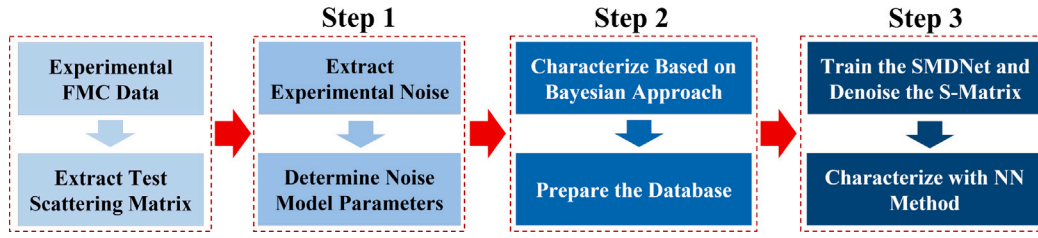


Fig. 8. The proposed defect characterization procedure based on the distortion model, Bayesian approach, and the SMDNet.

Table 6

The error metrics for size prediction of SMDNet and CBDNet on different noise parameters.

Noise Params	Method	R2	MAE (λ)	RMSE (λ)	EVS
$\lambda_1 = 45^\circ$	SMDNet	0.9384	0.0237	0.1144	0.9385
$\lambda_2 = 20^\circ$	CBDNet [28]	0.8366	0.0592	0.1863	0.8366
$\lambda_1 = 25^\circ$	SMDNet	0.9316	0.0268	0.1206	0.9318
$\lambda_2 = 20^\circ$	CBDNet [28]	0.8518	0.0573	0.1775	0.8524
$\lambda_1 = 40^\circ$	SMDNet	0.9881	0.0053	0.0503	0.9881
$\lambda_2 = 40^\circ$	CBDNet [28]	0.9917	0.0046	0.0421	0.9917

Table 7

The error metrics for angle prediction of SMDNet and CBDNet with different noise parameters.

Noise Params	Method	R2	MAE ($^\circ$)	RMSE ($^\circ$)	EVS
$\lambda_1 = 45^\circ$	SMDNet	0.9585	0.6458	2.3330	0.9587
$\lambda_2 = 20^\circ$	CBDNet [28]	0.9031	1.3438	3.5667	0.9031
$\lambda_1 = 25^\circ$	SMDNet	0.9515	0.7214	2.5233	0.9519
$\lambda_2 = 20^\circ$	CBDNet [28]	0.9188	1.2057	3.2636	0.9197
$\lambda_1 = 40^\circ$	SMDNet	0.9919	0.1732	1.0301	0.9919
$\lambda_2 = 40^\circ$	CBDNet [28]	0.9913	0.1745	1.0704	0.9913

Table 8

Sizes and angles of the defects in the test specimen.

Notch	1	2	3	4	5	6
Size (λ)	0.8	0.8	1.2	1.2	1.6	1.6
Angle ($^\circ$)	60	75	60	75	60	75

as 1.2λ and 60° , respectively, based on this result. In addition, the difference between the two scattering matrices (*i.e.*, the reconstruction error) is small (within 0.01) for all incident and scattering angles as shown in Fig. 7(d). In general, it can be seen that the SMDNet has good denoising performance on the simulated data. Note that the results in Fig. 7 were obtained for a positive-angled (60°) crack using a training set containing only positive-angled cracks. However, the determination of an appropriate database composition for a test scattering matrix is not straightforward in practice, and a solution to this problem is provided in Section 4.

4. Experimental results

In this section, the denoising and characterization performance of the proposed SMDNet-based method is further studied via experiments. A 2.5 MHz, 64 element array with an element pitch of 0.5 mm was used and the defects (slots with a small width of 0.2 mm) in Table 8 were manufactured using wire electrical discharge machining (WEDM). The scattering matrix was extracted from experimental FMC data using the reversible imaging algorithm [43]. Note that the same measurement configuration was adopted in all experiments (*i.e.*, the defect is located at the array center at a vertical distance of 20 mm).

Fig. 8 shows the characterization procedure developed in this study which consists of three steps. Step 2 (the Bayesian approach) and Step 3 (the SMDNet) were discussed in Section 2; here, the approach for determining the noise parameters (Section 4.1) is first introduced, and then

the experimental results, along with an analysis of the characterization uncertainty, are presented (Section 4.2).

4.1. Determination of the noise parameters

Because the noise parameters have a key impact on the denoising performance of the SMDNet, an approach for determining the noise parameters given an experimental measurement was implemented in this section. First, a coherent noise database was prepared, which covered all possible noise parameter values. In particular, because we are mainly interested in characterizing inclined cracks with large orientation angles, and the amplitude of the scattering matrix is often small in such cases, the noise RMS roughness σ was set as 0.05. The considered correlation length range was $[5^\circ, 45^\circ]$, and λ_1 and λ_2 were sampled in 5° intervals. This gave 81 different $[\lambda_1, \lambda_2]$ pairs, and 500 realizations of noise were simulated for each set of the noise parameters. In total, the coherent noise database contained 40,500 noise samples.

Subsequently, a parametric manifold mapping approach (PMMA) based on PCA [25] was adopted to obtain an estimation of the experimental noise. As illustrated in Fig. 9(a), this method aimed to find the characterization result by projecting a noisy scattering matrix s_n onto the defect manifold, which represents the set of ideal noise-free scattering matrices of cracks [17]. The estimated noise vector can be obtained from this result as $\hat{n} = s_n - s_o$, where s_o denotes the projection point of s_n on the defect manifold. In practice, the problem of finding the projection point s_o can be solved by searching for the minimum distance between s_n and each triangular facet of the defect manifold. The flowchart of the PMMA implementation adopted in this study is shown in Fig. 9(b), and interested readers may refer to Ref. [25] for further details about this approach.

Finally, the noise parameters were determined by finding the nearest neighbor of the estimated noise \hat{n} in the coherent noise database. The mean structural similarity index (MSSIM) [44] was used as the distance metric, which is defined as:

$$\text{MSSIM} = \frac{1}{N} \sum_{k=1}^N \text{SSIM}(x_k, y_k) \quad (19)$$

In Eq. (19), N is the number of sliding windows over which the SSIM score is averaged, while x_k and y_k refer to the k th image blocks of two images x and y . The SSIM of the two images is defined as:

$$\text{SSIM}(x, y) = l(x, y) * c(x, y) * s(x, y) \quad (20)$$

In the above equation, l , c , and s denote the similarity of two images, x and y , evaluated in terms of their brightness, contrast, and structure, respectively.

Figs. 10(a)–(d) show the experimental noises and their nearest neighbor results for 1.6λ , 60° and 0.8λ , 75° cracks. Here, the MSSIM metric is used. These results show both the amplitude and shape pattern of the experimental noise can be well represented by the simulated distortion with properly chosen noise parameters. In Section 4.2, the noise parameters obtained by the proposed approach were used to train the SMDNet for each set of test data.

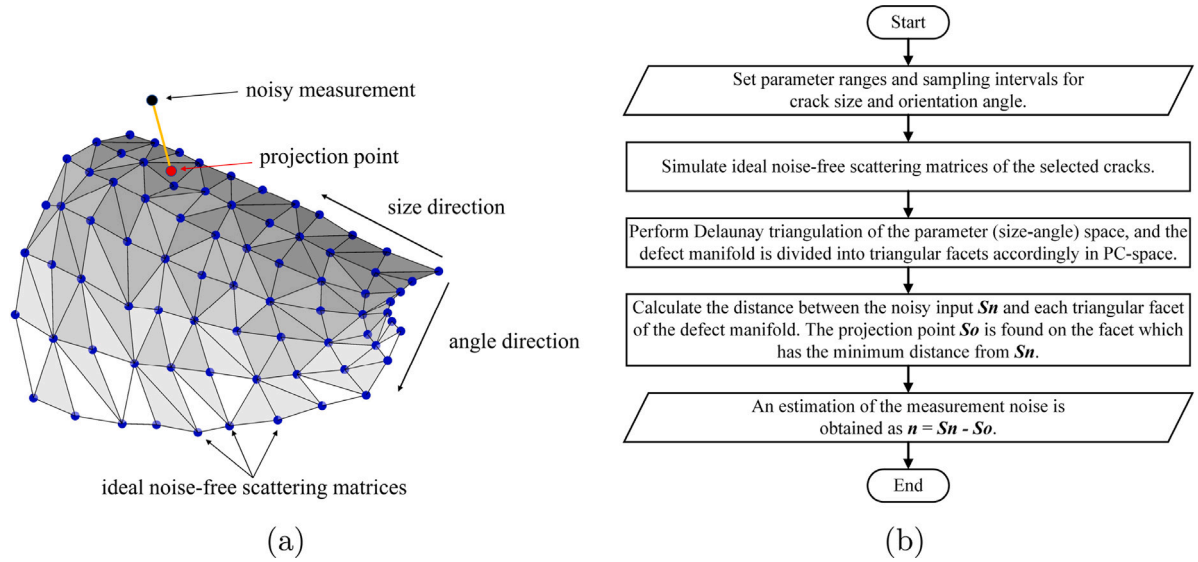


Fig. 9. (a) Illustration of the parametric manifold mapping approach (PMMA), and (b) flowchart of the PMMA implementation [25].

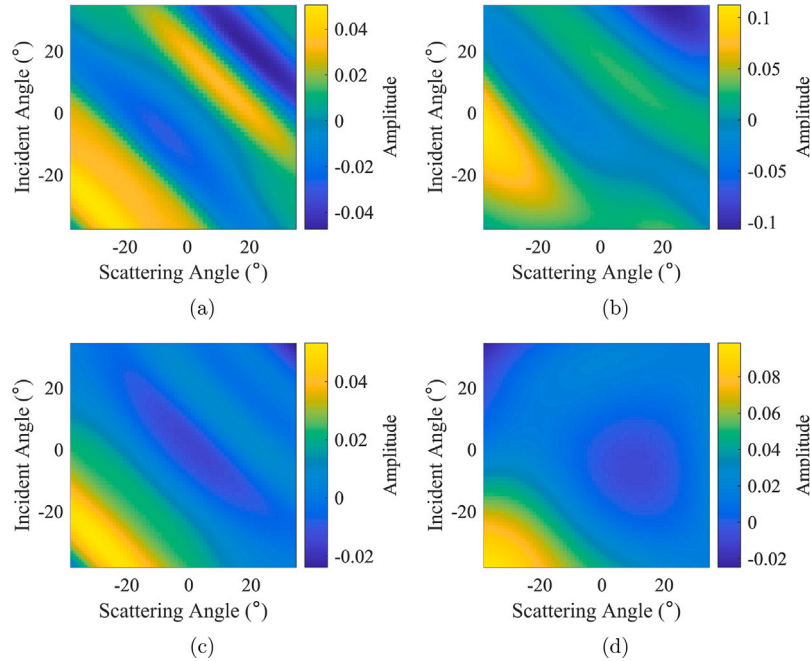


Fig. 10. The nearest neighbor results of experimental noises obtained using the MSSIM metric: (a)–(b) the experimental noise and its nearest neighbor of a 1.6 λ , 60° crack, and (c)–(d) the experimental noise and its nearest neighbor of a 0.8 λ , 75° crack.

4.2. Characterization results and uncertainty analysis

It was previously shown that the characterization uncertainty obtained by the Bayesian approach was low for favorably oriented defects [20]. For the experimental configuration adopted in this study, the Bayesian approach was found to perform well if the crack orientation angle was within 45°, and hence, we focused on the characterization of cracks which have orientation angles greater than 45° in this section (see Table 8).

Figs. 11(a)–(f) show the characterization results of Notches 1–6 in the test specimens, obtained by the conventional Bayesian approach. The noise parameters (shown in Table 9) were determined by the method proposed in Section 4.1. The results in Figs. 11(b), (c), and (f) show that the red dots (*i.e.*, true parameter points) are close to the

maximum probability points. On the other hand, the characterization results of Notches 1, 4, and 5 have large errors. Although, the Bayesian approach also exhibited its robustness by identifying the true parameter points as secondary peaks.

These results show that all the cracks were classified accurately as far as the crack angle was concerned (*i.e.*, positive versus negative angles). The values in Table 9 indicate the proportion of the positive angles given by the Bayesian approach (*i.e.*, sum of the probabilities of positive-angled cracks). In principle, this value determines the proportion of the positive-angled cracks in the database used for training the SMDNet. Since the values shown in Table 9 are all very large (above 0.95), the database contained cracks with positive angles only when training the SMDNet. Despite excellent performance in the classification of the crack angle, the results in Fig. 11 also confirm

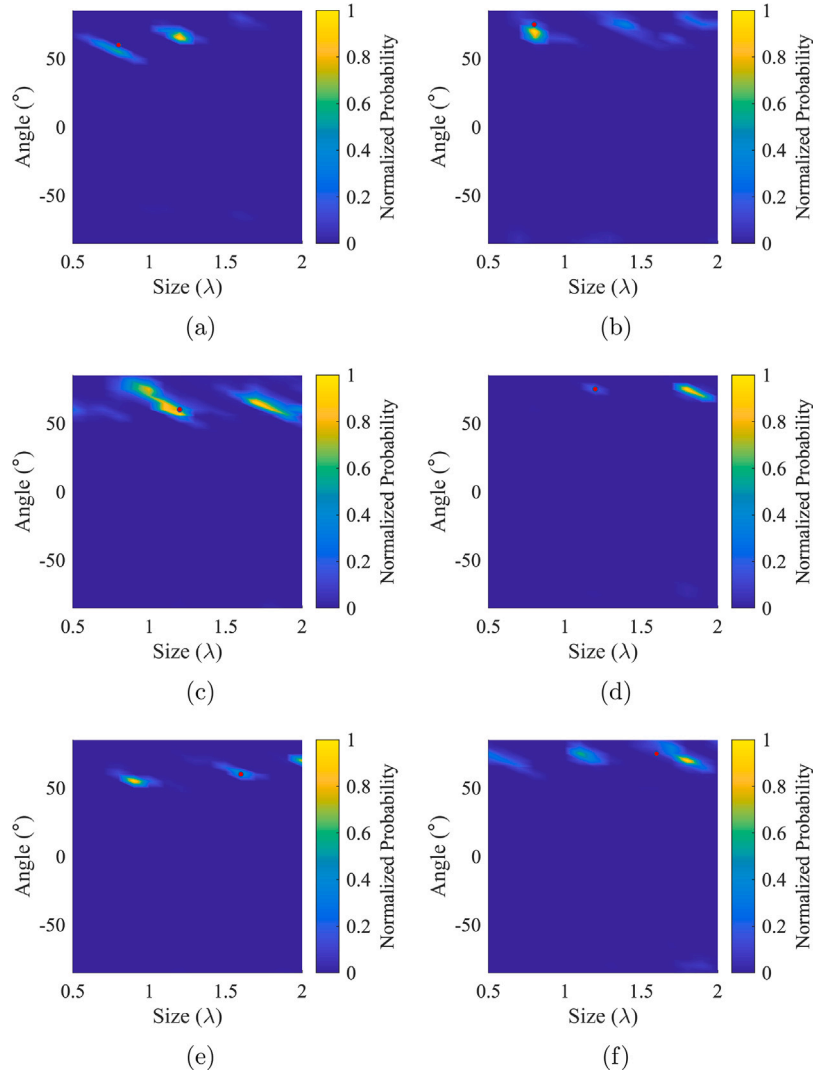


Fig. 11. The characterization results of the experimental data obtained with the Bayesian approach, demonstrating high characterization uncertainty. The crack parameters are: (a) 0.8λ , 60° , (b) 0.8λ , 75° , (c) 1.2λ , 60° , (d) 1.2λ , 75° , (e) 1.6λ , 60° , and (f) 1.6λ , 75° , respectively. Note that the noise parameters used in the Bayesian approach were determined by the method proposed in Section 4.1.

Table 9

The estimated noise parameters and proportions of the positive angles of experimental measurements.

Notch	1	2	3	4	5	6
λ_1	35°	40°	25°	45°	45°	30°
λ_2	30°	40°	20°	20°	15°	45°
Proportion	0.9911	0.9657	0.9958	0.9770	0.9907	0.9721

that the Bayesian approach suffers from high uncertainty in size when characterizing unfavorably oriented cracks.

Two denoised results of the experimental measurements are shown in Figs. 12 and 13. Fig. 12(a) shows the test scattering matrix of a 1.2λ , 60° crack extracted from experimental FMC data. The structure of the scattering matrix is shown to be distorted by experimental noise. The denoised result given by the SMDNet (see Fig. 12(b)) approached the ideal scattering matrix in Fig. 12(c), and the difference between the denoised and ideal scattering matrix was small (see Fig. 12(d)). Moreover, Fig. 13 demonstrates that the information-rich part of the scattering matrix (i.e., the top right corner) can be well restored for the 1.6λ , 60° crack, which is crucial for its characterization. Compared to the ideal scattering matrices in Figs. 12(c) and 13(c), the relative Euclidean distances defined as $\|s_n - s_p\|_2 / \|s_p\|_2$ were 0.31 and 0.41

for the 1.2λ , 60° and 1.6λ , 60° cracks, respectively. After denoising by the SMDNet, the relative Euclidean distances reduced to 0.22 and 0.17; thus, it is expected that the characterization accuracy can be improved by applying the nearest neighbor approach to the denoised results.

In order to evaluate the characterization uncertainty, 400 noisy measurements were prepared for each test defect by contaminating the experimental measurement with different realizations of noise (see Eq. (18)). The noise realizations were different from those used to train the SMDNet model. Each noisy measurement was first processed by the proposed SMDNet model, and then the nearest neighbor approach was used to characterize the denoised scattering matrix.

Figs. 14(a)–(f) show the 2-D histogram plots of the defect parameters obtained using this method. The true defect parameters are shown as the red points, which are close to the maximum probability points in all these results. The green points correspond to the characterization results of the original experimental data, and they are shown to be accurately characterized. Tables 10 and 11 summarize the RMSE (see Eq. (14)) results of Notches 1–6 and support the conclusion that the proposed procedure has produced more accurate results with lower uncertainty for Notches 2–6. Although the original Bayesian approach gave a lower RMSE in size for Notch 1, the probability peak of Fig. 11(a) is far from the true parameter point, as opposed to the single dominant peak of Fig. 14(a), which has a small error. Meanwhile, the

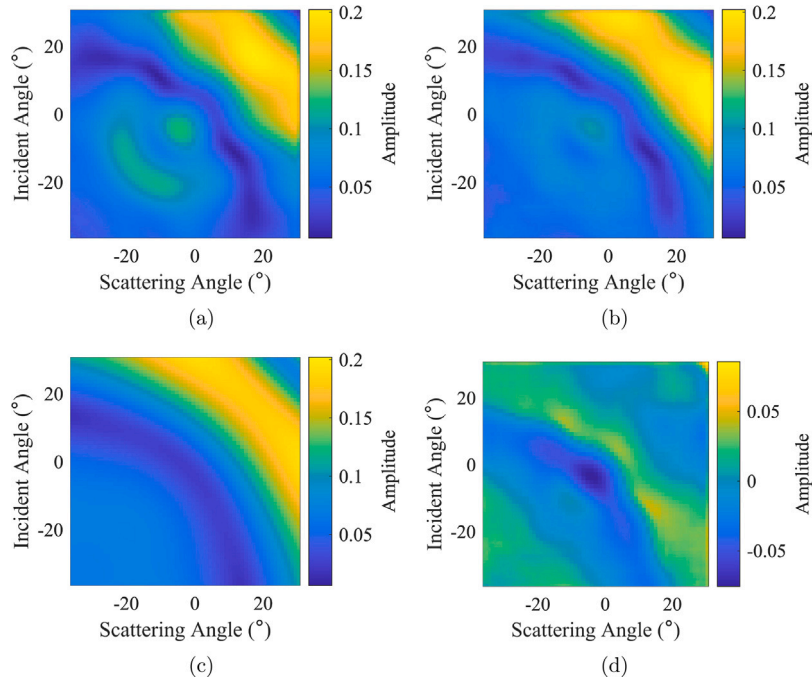


Fig. 12. The experimental measurements of Notch 3: (a) noisy scattering matrix, (b) denoised scattering matrix, (c) ideal scattering matrix, and (d) difference between the denoised and ideal scattering matrix. The defect parameters are 1.2λ and 60° .

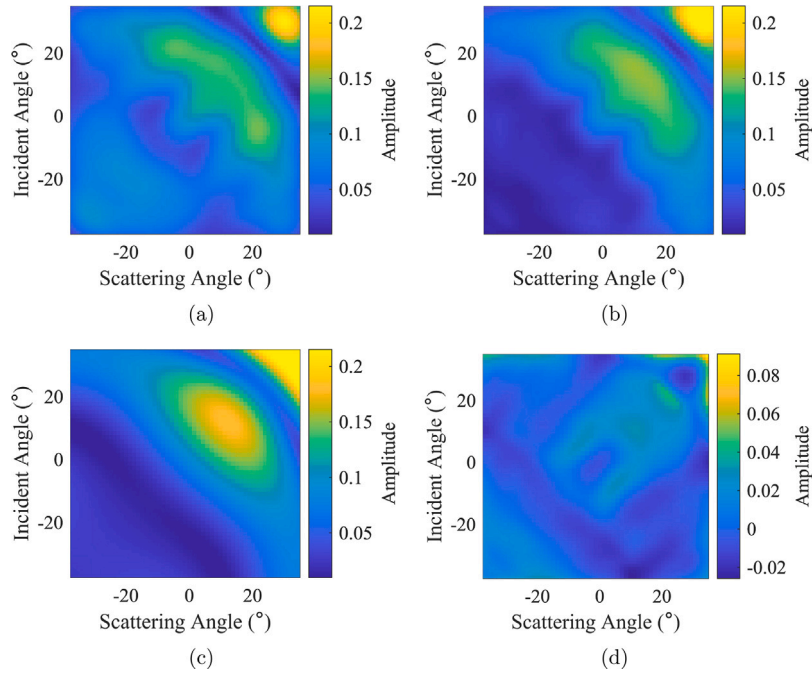


Fig. 13. The experimental measurements of Notch 5: (a) noisy scattering matrix, (b) denoised scattering matrix, (c) ideal scattering matrix, and (d) difference between the noisy and de-noised scattering matrices. The defect parameters are 1.6λ and 60° .

CBDNet suffers from high uncertainty, although it has obtained better results than NAFNet for simulation data, which suggests that CBDNet's noise estimation network has insufficient perception capability in an actual measurement environment. To summarize, the proposed SMDNet achieved four of the best (and one second-best) characterization results on experimental data.

5. Conclusions

In this paper, the problem of characterizing crack-like defects with large orientation angles was studied. The use of a scattering matrix was explored, and we focused on recovering the ideal noise-free scattering

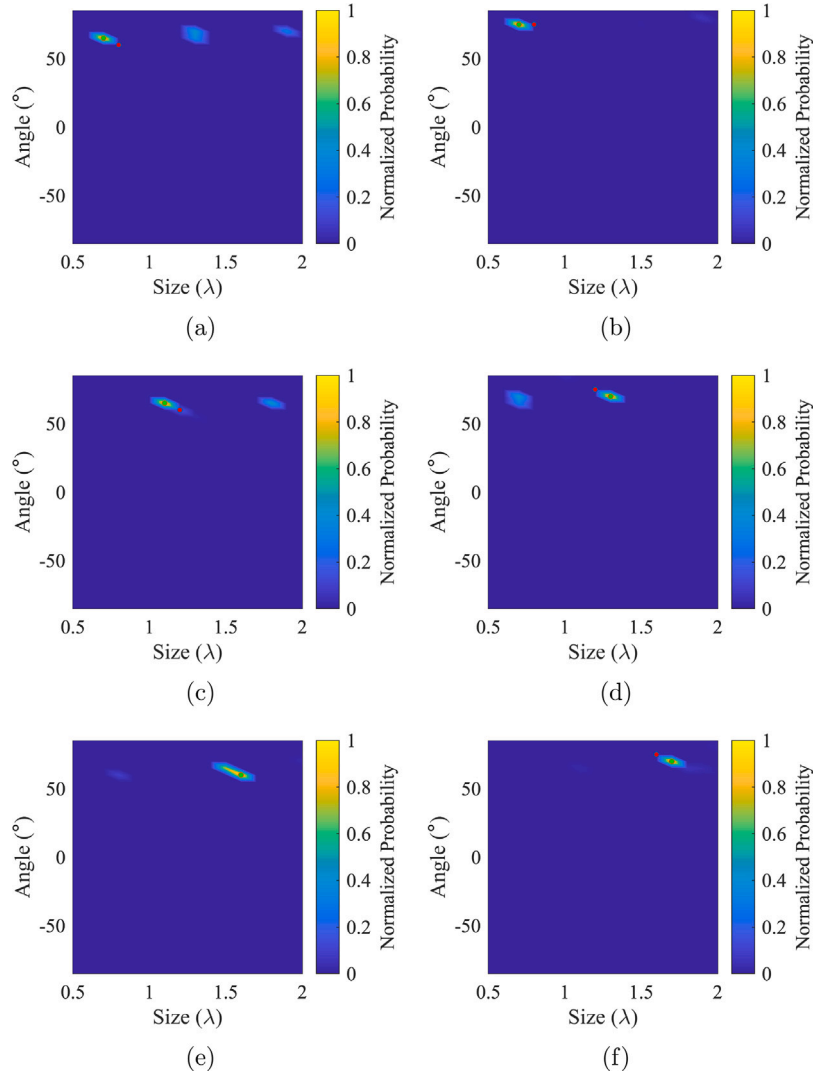


Fig. 14. The characterization results of the experimental data with uncertainty analysis, where the crack parameters are: (a) 0.8λ , 60° , (b) 0.8λ , 75° , (c) 1.2λ , 60° , (d) 1.2λ , 75° , (e) 1.6λ , 60° , and (f) 1.6λ , 75° . The green points denote the characterization results of the original measurement, and the red dots are the true parameters. In (e), the red point is overlapped with the green point. (For interpretation of the references to color in this figure legend, the reader is referred to the web version of this article.)

Table 10
RMSE results (in wavelengths) for size prediction of different methods.

Notch	PCA [24]	PMMA [25]	Bayesian [25]	NAFNet [38]	CBDNet [28]	SMDNet
1	0.3321	0.3430	0.3783	0.4380	0.7248	0.5267
2	0.3943	0.3452	0.4715	0.5353	0.3769	0.2735
3	0.3552	0.1912	0.4134	0.1114	0.3098	0.1039
4	0.3688	0.3680	0.5584	0.4803	0.3586	0.3361
5	0.5532	0.5288	0.5125	0.4700	0.1431	0.1943
6	0.3664	0.3959	0.5173	0.3013	0.3114	0.1424

Table 11
RMSE results (in degrees) for angle prediction of different methods.

Notch	PCA [24]	PMMA [25]	Bayesian [25]	NAFNet [38]	CBDNet [28]	SMDNet
1	10.7761	23.6736	14.1104	5.2619	8.5073	7.1851
2	9.6144	10.0156	30.2049	7.2457	5.2202	1.199
3	8.0739	21.4622	12.9182	7.7096	8.3629	6.1847
4	10.1427	10.6888	22.8636	7.8382	15.7023	6.245
5	11.3054	13.5000	14.7073	7.4372	5.2142	3.3727
6	9.7404	9.4406	26.4571	6.0415	9.9812	5.6624

matrix of a defect from one contaminated by noise. Given an experimental measurement, a parametric manifold mapping approach was first used to determine the noise parameters of the test data. Then, a deep neural network (SMDNet), specifically designed for scattering matrix denoising, was constructed with a custom asymmetric loss function. The performance of the proposed method was demonstrated through simulations and experiments for characterization of inclined crack-like defects with orientation angles greater than 45° . When applied to six experimentally measured scattering matrices of crack-like defects, the mean RMSE of size was 0.2628λ for the proposed method; this is much lower than the RMSE of a benchmark Bayesian approach (0.4752λ).

However, it is still an indispensable part of the proposed method to find a specific distortion model parameter with PMMA for different experimental measurements. Hence, a promising area of future work may be the combination of defect data with a distortion model to build a physics-informed neural network for noise parameter estimation. Like other deep learning methods, the SMDNet can potentially encounter the situation in which the experimental measurements are distributed differently from the simulation data. Although the PMMA was implemented in this study for an accurate estimation of noise parameters, it is still possible that the noise in the actual measurement is out-of-distribution (OOD). Therefore, it is important to quantify the uncertainty in the characterization results and improve the characterization

robustness of the OOD measurements. Moreover, the optimization of the network structure and hyperparameters adopted in this work (details are provided in the supplemental material) was time-consuming, and it would be necessary to propose more efficient noise estimation methods and denoising networks for their widespread applications in the industry sector.

The scattering-matrix-based method offers a promising way of characterizing small crack-like defects with large orientation angles. The current work marks a step forward in applying deep denoising neural networks to real-world problems of ultrasonic NDT. The so-called SMDNet can restore the noise-free scattering matrix from the noisy measurement, which helps an operator to gain an intuitive understanding as to whether the defect belongs to the known types of defects. The proposed method is also shown to be capable of reducing the characterization uncertainty in noisy environments; thus, it can be implemented by modern UT equipment for better inspection performance.

CRedit authorship contribution statement

Changrong Guo: Methodology, Software, Validation, Formal analysis, Writing – original draft, Writing – review & editing, Visualization. **Junjie Ren:** Methodology, Investigation, Resources. **Jianfeng Xu:** Conceptualization, Project administration, Funding acquisition. **Long Bai:** Conceptualization, Methodology, Formal analysis, Investigation, Writing – original draft, Writing – review & editing, Project administration, Funding acquisition.

Declaration of competing interest

The authors declare that they have no known competing financial interests or personal relationships that could have appeared to influence the work reported in this paper.

Data availability

Data will be made available on request.

Acknowledgment

This work was supported by National Natural Science Foundation of China under grant numbers 52005205 and 52188102, and the National Science Fund for Distinguished Young Scholars, China under grant number 52225506.

Appendix A. Supplementary data

Supplementary material related to this article can be found online at <https://doi.org/10.1016/j.ndteint.2023.102813>.

References

- [1] Achenbach JD. Quantitative nondestructive evaluation. *Int J Solids Struct* 2000;37(1):13–27. [https://doi.org/10.1016/S0020-7683\(99\)00074-8](https://doi.org/10.1016/S0020-7683(99)00074-8).
- [2] Ni X, Ma Z, Liu J, Shi B, Liu H. Attention network for rail surface defect detection via consistency of intersection-over-union(IoU)-guided center-point estimation. *IEEE Trans Ind Inf* 2022;18(3):1694–705. <https://doi.org/10.1109/TII.2021.3085848>.
- [3] Wu Q, Qin X, Dong K, Shi A, Hu Z. A learning-based crack defect detection and 3D localization framework for automated fluorescent magnetic particle inspection. *Expert Syst Appl* 2023;214:118966. <https://doi.org/10.1016/j.eswa.2022.118966>.
- [4] Bai H, Guo D, Wang W, Tan X, Yan M, Chen G, et al. Experimental investigation on flexural behavior of steel-concrete composite floor slabs with distributed fiber optic sensors. *J Build Eng* 2022;54:104668. <https://doi.org/10.1016/j.jobe.2022.104668>.
- [5] Tan X, Bao Y. Measuring crack width using a distributed fiber optic sensor based on optical frequency domain reflectometry. *Measurement* 2021;172:108945. <https://doi.org/10.1016/j.measurement.2020.108945>.
- [6] Yan M, Tan X, Mahjoubi S, Bao Y. Strain transfer effect on measurements with distributed fiber optic sensors. *Autom Constr* 2022;139:104262. <https://doi.org/10.1016/j.autcon.2022.104262>.
- [7] Tan X, Abu-Obeidah A, Bao Y, Nassif H, Nasreddine W. Measurement and visualization of strains and cracks in CFRP post-tensioned fiber reinforced concrete beams using distributed fiber optic sensors. *Autom Constr* 2021;124:103604. <https://doi.org/10.1016/j.autcon.2021.103604>.
- [8] Liu Y, Tian G, Gao B, Lu X, Li H, Chen X, et al. Depth quantification of rolling contact fatigue crack using skewness of eddy current pulsed thermography in stationary and scanning modes. *NDT E Int* 2022;128:102630. <https://doi.org/10.1016/j.ndteint.2022.102630>.
- [9] Chai M, Hou X, Zhang Z, Duan Q. Identification and prediction of fatigue crack growth under different stress ratios using acoustic emission data. *Int J Fatigue* 2022;160:106860. <https://doi.org/10.1016/j.ijfatigue.2022.106860>.
- [10] Kundu T. Ultrasonic nondestructive evaluation: engineering and biological material characterization. Boca Raton, FL: CRC Press; 2004.
- [11] Bray DE, Stanley RK. Nondestructive evaluation: a tool in design, manufacturing and service. Boca Raton, FL: CRC Press; 1997.
- [12] Yin X, Shi F. Hybrid geometrical full waveform inversion for ultrasonic defect characterisation. *J Sound Vib* 2022;535:117099. <https://doi.org/10.1016/j.jsv.2022.117099>.
- [13] Zhu W, Xiang Y, Zhang H, Cheng Y, Fan G, Zhang H. Research on ultrasonic sparse DC-TFM imaging method of rail defects. *Measurement* 2022;200:111690. <https://doi.org/10.1016/j.measurement.2022.111690>.
- [14] Ha JM, Seung HM, Choi W. Autoencoder-based detection of near-surface defects in ultrasonic testing. *Ultrasonics* 2022;119:106637. <https://doi.org/10.1016/j.ultras.2021.106637>.
- [15] Blitz J, Simpson G. Ultrasonic methods of non-destructive testing, Vol. 2. London, UK: Chapman & Hall; 1996.
- [16] Drinkwater BW, Wilcox PD. Ultrasonic arrays for non-destructive evaluation: A review. *NDT E Int* 2006;39(7):525–41. <https://doi.org/10.1016/j.ndteint.2006.03.006>.
- [17] Holmes C, Drinkwater BW, Wilcox PD. Post-processing of the full matrix of ultrasonic transmit–receive array data for non-destructive evaluation. *NDT E Int* 2005;38(8):701–11. <https://doi.org/10.1016/j.ndteint.2005.04.002>.
- [18] Le Jeune L, Robert S, Lopez Villaverde E, Prada C. Plane wave imaging for ultrasonic non-destructive testing: Generalization to multimodal imaging. *Ultrasonics* 2016;64:128–38. <https://doi.org/10.1016/j.ultras.2015.08.008>.
- [19] Zhang J, Drinkwater BW, Wilcox PD. The use of ultrasonic arrays to characterize crack-like defects. *J Nondestruct Eval* 2010;29(4):222–32. <https://doi.org/10.1007/s10921-010-0080-6>.
- [20] Bai L, Le Bourdais F, Miorelli R, Calmon P, Velichko A, Drinkwater BW. Ultrasonic defect characterization using the scattering matrix: A performance comparison study of Bayesian inversion and machine learning schemas. *IEEE Trans Ultrason Ferroelectr Freq Control* 2021;68(10):3143–55. <https://doi.org/10.1109/TUFFC.2021.3084798>.
- [21] Elliott JB, Lowe MJS, Huthwaite P, Phillips R, Duxbury DJ. Sizing subwavelength defects with ultrasonic imagery: An assessment of super-resolution imaging on simulated rough defects. *IEEE Trans Ultrason Ferroelectr Freq Control* 2019;66(10):1634–48. <https://doi.org/10.1109/TUFFC.2019.2925974>.
- [22] Zhang J, Drinkwater BW, Wilcox PD. Defect characterization using an ultrasonic array to measure the scattering coefficient matrix. *IEEE Trans Ultrason Ferroelectr Freq Control* 2008;55(10):2254–65. <https://doi.org/10.1109/TUFFC.2008.924>.
- [23] Bai L, Velichko A, Drinkwater BW. Characterization of defects using ultrasonic arrays: A dynamic classifier approach. *IEEE Trans Ultrason Ferroelectr Freq Control* 2015;62(12):2146–60. <https://doi.org/10.1109/TUFFC.2015.007334>.
- [24] Bai L, Velichko A, Drinkwater BW. Ultrasonic characterization of crack-like defects using scattering matrix similarity metrics. *IEEE Trans Ultrason Ferroelectr Freq Control* 2015;62(3):545–59. <https://doi.org/10.1109/TUFFC.2014.006848>.
- [25] Velichko A, Bai L, Drinkwater BW. Ultrasonic defect characterization using parametric-manifold mapping. *Proc R Soc A Math Phys Eng Sci* 2017;473(2202):20170056. <https://doi.org/10.1098/rspa.2017.0056>.
- [26] Zhang K, Zuo W, Chen Y, Meng D, Zhang L. Beyond a Gaussian denoiser: Residual learning of deep CNN for image denoising. *IEEE Trans Image Process* 2017;26(7):3142–55. <https://doi.org/10.1109/TIP.2017.2662206>.
- [27] Zhang K, Zuo W, Zhang L. Ffdnet: Toward a fast and flexible solution for CNN-based image denoising. *IEEE Trans Image Process* 2018;27(9):4608–22. <https://doi.org/10.1109/TIP.2018.2839891>.
- [28] Guo S, Yan Z, Zhang K, Zuo W, Zhang L. Toward convolutional blind denoising of real photographs. 2019, <https://doi.org/10.48550/arXiv.1807.04686>, arXiv:1807.04686.
- [29] Gao F, Hua J. Damage characterization using CNN and SAE of broadband lamb waves. *Ultrasonics* 2022;119:106592. <https://doi.org/10.1016/j.ultras.2021.106592>.
- [30] Miorelli R, Fisher C, Kulakovskiy A, Chapuis B, Mesnil O, D’Almeida O. Defect sizing in guided wave imaging structural health monitoring using convolutional neural networks. *NDT E Int* 2021;122:102480. <https://doi.org/10.1016/j.ndteint.2021.102480>.

- [31] Ronneberger O, Fischer P, Brox T. U-net: convolutional networks for biomedical image segmentation. In: International conference on medical image computing and computer-assisted intervention. Springer; 2015, p. 234–41.
- [32] Bai L, Velichko A, Clare AT, Dryburgh P, Pieris D, Drinkwater BW. The effect of distortion models on characterisation of real defects using ultrasonic arrays. *NDT E Int* 2020;113:102263. <http://dx.doi.org/10.1016/j.ndteint.2020.102263>.
- [33] Shi F, Choi W, Lowe MJS, Skelton EA, Craster RV. The validity of Kirchhoff theory for scattering of elastic waves from rough surfaces. *Proc R Soc A Math Phys Eng Sci* 2015;471(2178):20140977. <http://dx.doi.org/10.1098/rspa.2014.0977>.
- [34] Hastie T, Tibshirani R, Friedman JH. The elements of statistical learning: data mining, inference, and prediction, Vol. 2. New York, NY: Springer; 2001.
- [35] Long J, Shelhamer E, Darrell T. Fully convolutional networks for semantic segmentation. In: 2015 IEEE conference on computer vision and pattern recognition. Boston, MA, USA: IEEE; 2015, p. 3431–40. <http://dx.doi.org/10.1109/CVPR.2015.7298965>.
- [36] Chang M, Li Q, Feng H, Xu Z. Spatial-adaptive network for single image denoising. 2020, arXiv [arXiv:2001.10291](https://arxiv.org/abs/2001.10291).
- [37] Zamir SW, Arora A, Khan S, Hayat M, Khan FS, Yang M-H, et al. Learning enriched features for real image restoration and enhancement. 2020, arXiv [arXiv:2003.06792](https://arxiv.org/abs/2003.06792).
- [38] Chen L, Chu X, Zhang X, Sun J. Simple baselines for image restoration. 2022, arXiv [arXiv:2204.04676](https://arxiv.org/abs/2204.04676).
- [39] Wang Z, Cun X, Bao J, Zhou W, Liu J, Li H. Uformer: A general U-shaped transformer for image restoration. 2021, arXiv [arXiv:2106.03106](https://arxiv.org/abs/2106.03106).
- [40] Zamir SW, Arora A, Khan S, Hayat M, Khan FS, Yang M-H. Restormer: efficient transformer for high-resolution image restoration. 2022, arXiv [arXiv:2111.09881](https://arxiv.org/abs/2111.09881).
- [41] Glushkov E, Glushkova N, Ekhlakov A, Shapar E. An analytically based computer model for surface measurements in ultrasonic crack detection. *Wave Mot Int J Report Res Wave Phenomena* 2006;43(6):458–73. <http://dx.doi.org/10.1016/j.wavemoti.2006.03.002>.
- [42] Jolliffe IT. Principal component analysis. Springer, 2nd ed.. New York, NY: Springer-Verlag; 2002, <http://dx.doi.org/10.1007/b98835>.
- [43] Velichko A, Wilcox P. Reversible back-propagation imaging algorithm for post-processing of ultrasonic array data. *IEEE Trans Ultrason Ferroelectr Freq Control* 2009;56(11):2492–503. <http://dx.doi.org/10.1109/TUFFC.2009.1336>.
- [44] Wang Z, Lu L, Bovik AC. Video quality assessment based on structural distortion measurement. *Signal Process, Image Commun* 2004;19(2):121–32. [http://dx.doi.org/10.1016/S0923-5965\(03\)00076-6](http://dx.doi.org/10.1016/S0923-5965(03)00076-6).